Railway Engineering Science (2024) 32(1):20–35
https://doi.org/10.1007/s40534-023-00316-2

Influence of railway wheel tread damage on wheel–rail impact loads and the durability of wheelsets

Michele Maglio[1] · Tore Vernersson[1] · Jens C. O. Nielsen[1] · Anders Ekberg[1] · Elena Kabo[1]

Received: 4 April 2023 / Revised: 10 July 2023 / Accepted: 12 July 2023 / Published online: 16 August 2023

Abstract
Dynamic wheel–rail contact forces induced by a severe form of wheel tread damage have been measured by a wheel impact load detector during full-scale field tests at different vehicle speeds. Based on laser scanning, the measured three-dimensional damage geometry is employed in simulations of dynamic vehicle–track interaction to calibrate and verify a simulation model. The relation between the magnitude of the impact load and various operational parameters, such as vehicle speed, lateral position of wheel–rail contact, track stiffness and position of impact within a sleeper bay, is investigated. The calibrated model is later employed in simulations featuring other forms of tread damage; their effects on impact load and subsequent fatigue impact on bearings, wheel webs and subsurface initiated rolling contact fatigue of the wheel tread are assessed. The results quantify the effects of wheel tread defects and are valuable in a shift towards condition-based maintenance of running gear, and for general assessment of the severity of different types of railway wheel tread damage.

Keywords Wheel tread damage · Rolling contact fatigue cluster · Field measurements · Dynamic vehicle–track interaction · Wheel–rail impact load · Wheelset durability

1 Introduction

Railway vehicles with wheels affected by tread (rolling surface) damage leading to unacceptably high vertical dynamic wheel–rail contact forces must be taken out of service. This causes traffic disruptions and is a major cause of train delays in the Swedish railway network during the coldest months of the year [1, 2]. One reason for the application of load limits is that impact loads generated by wheel tread irregularities, such as wheel flats and rolling contact fatigue (RCF) clusters, result in high stresses in vehicle components, wheels, axles and bearings, thus increasing the risk of fatigue failures [3]. However, even wheel loads not exceeding the limits might result in substantial dynamic contributions to stresses and influence fatigue life, as will be investigated in the current study.

In addition, impact forces due to such wheel tread defects may shorten the life of track components, such as rails and sleepers, resulting in higher costs for maintenance of infrastructure [4]. Different forms of wheel out-of-roundness (OOR) can also cause increased levels of rolling noise, impact noise and ground-borne vibration [5, 6], as well as higher vibration levels of bearings and axle boxes [7, 8].

Wheel tread damage, or more generally, wheel out-of-roundness is generated by different mechanisms (crack propagation, wear, ratchetting, etc.) that can promote and/or compete with each other [9]. Some of the forms of wheel tread damage that are frequently observed in Sweden are presented in Sect. 2. Wheel tread damage can be detected indirectly using different techniques, e.g. by measuring dynamic wheel–rail contact forces using wheel impact load detectors (WILDs) [1, 10, 11]. Based on WILD data, impact load variations over time were analysed to distinguish wheels with high or low probability of causing failures [12]. During periodic maintenance, wheel damage can be detected directly by visual inspection [13]; however, this method is human factor dependent. Research has been performed in developing artificial intelligence (AI) based methods to detect wheel tread damage, see for example [14] and [15].

Damage on the wheel tread can accelerate wheelset deterioration. Knowledge on how wheel tread damage evolves over time and which subsequent effects it will have on

✉ Michele Maglio
michele.maglio@chalmers.se

[1] CHARMEC, Department of Mechanical and Maritime Sciences, Chalmers University of Technology, SE-412 96 Gothenburg, Sweden

wheel–rail interaction and on wheelset durability is of vital importance for maintenance planning. In [16], impact loads and axle stresses for different sizes of tread defects were numerically predicted in a parameter study, with defect geometries modelled using an ellipsoid function. The novel contribution of this work is to present and verify a method to predict the effects of three-dimensional (3D) scanned wheel tread damage on the durability of railway wheels, axles and bearings. In the first part of this paper, measured impact loads from a field test campaign are used to verify a model for simulation of dynamic vehicle–track interaction. Next, specific forms of wheel tread damage have been measured by means of 3D laser scans, post-processed and implemented in the simulation model. Finally, the model is used to study the influence of the different forms of tread damage on dynamic stresses and their effects on the durability of the wheelset.

The results of the studies presented in this work can be used to prioritise maintenance of running gear featuring out-of-round wheels. Moreover, the results can provide information useful at maintenance depots for understanding the severity of different forms of tread damage and how they influence service lives of vehicle and track. Such information can guide towards improved operational restrictions for trains with elevated wheel load magnitudes. These actions can generate significant savings as well as increased safety levels for train operators and infrastructure managers.

2 Wheel tread damage

A comprehensive overview of different types of wheel tread damage is presented in [17]. The work in [18] is focussed on commonly occurring forms of wheel tread damage under winter conditions, namely wheel flats and RCF clusters. In the current study, the geometry of tread defects have been scanned in connection with field tests and at maintenance workshops.

Wheel flats are generated when the wheel slides on the rail. Besides the severe abrasive wear, heating followed by rapid cooling may result in martensite formation over a section of the wheel tread, where the material becomes harder and more brittle. Subsequent mechanical loads may lead to material fall-out which aggravates the wheel flat. Newly formed wheel flats tend to have sharp edges, see Fig. 1a. These edges round off over time due to the repeated impacts on the rail, see Fig. 1b.

Vertical and tangential (creep) forces generated in the wheel–rail contact contribute to the initiation and growth of RCF cracks on the wheel tread. If networks of fatigue cracks grow and interact, material fall-out will occur. In some cases, the RCF damage clusters that then form are distributed over a large distance in the circumferential direction, or even along the entire wheel circumference, see Fig. 1c. RCF clusters are particularly common during the winter season [18].

Further, the wheel tread profile might change due to wear. Wear can also appear as periodic (polygonisation), stochastic or local variations in wheel radius around the circumference. One can note that RCF clusters (and wheel flats) are easily recognised by visual inspection of the wheel tread, whereas polygonisation often requires some type of measurement equipment to be identified.

The current study features investigations of wheels affected both by severe RCF damage and localised wear and plastic deformation. Wheels affected by wheel flats have not been studied in the present work. However, one of the main

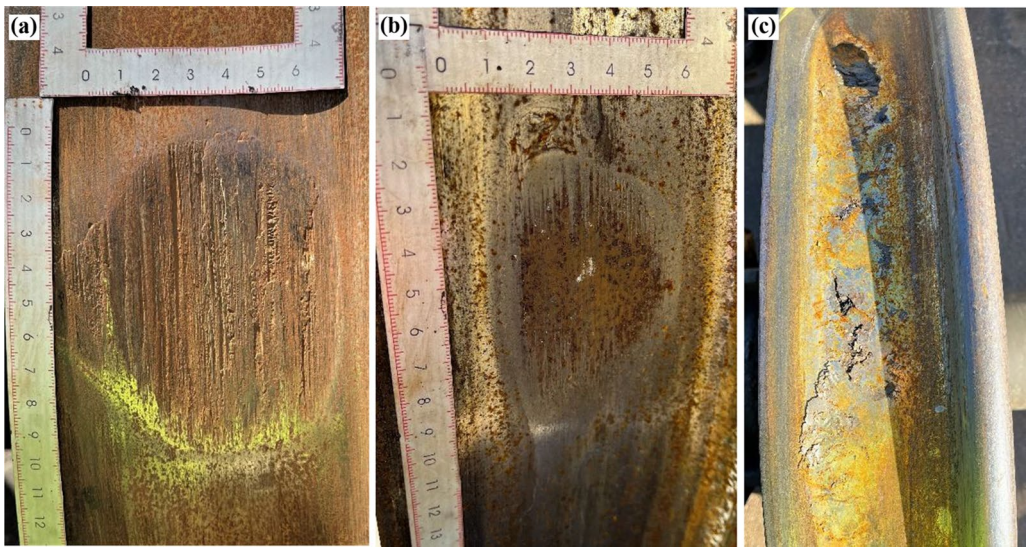

Fig. 1 Wheel tread with **a** a fresh wheel flat with sharp edges, **b** a wheel flat with rounded edges, and **c** RCF cluster

features of the simulation procedure demonstrated in this work is the ability to account for generic shapes and sizes of wheel tread damage including wheel flats. The geometry of damaged wheel treads has been characterised by 3D laser scanning measurements using the portable 3D laser equipment HandyScan [19]. The output from the 3D scanner is post-processed using VXinspect [19] and MATLAB [20]. The scanner has a maximum measurement accuracy of 0.03 mm, which allows for a very detailed characterisation of tread defects.

3 Effects of operational conditions on wheel–rail impact loads generated by damaged wheels

3.1 Field test

In cooperation with Trafikverket (the Swedish transport administration) and SJ (the Swedish national railway operator), loads generated by a damaged wheel passing over an impact load detector at different speeds have been investigated [1, 2]. The field test was performed in April 2018 at Sunderbyn on the Iron Ore line in northern Sweden. The detector consisted of eight instrumented sleepers equipped with load cells at each rail seat. The detector was calibrated in April 2017.

The test featured a bidirectional train composed of three units: two locomotives (one for each traffic direction) and a passenger coach in the middle. One wheel on the passenger coach had previously generated loads that exceeded the alarm limit at another detector. The wheelset had therefore been taken out of service until used in these tests. The wheel that generated alarm loads featured several RCF clusters. The size, distribution and depth of these were varying non-uniformly over the running surface, see Fig. 2. The opposite wheel on the same axle did not show any serious forms of damage. Some minor wear was present, as well as several rounded indentations, but these were not expected to give any significant influence on measured load magnitudes [17]. The other wheels on the wagon did not show any significant form of damage.

The tread, flange and parts of the rim of the two wheels were mapped using the portable 3D optical laser scanner described in Sect. 2. The tread of the severely damaged wheel can be described by two damaged regions located on diametrically opposite sides. Each region is characterised by the presence of two major RCF clusters with depths up to 1.8 mm and several minor defects [1].

The scanned wheel tread damage, see Fig. 2c, was used to generate a 3D mesh containing the distribution of radial deviation from the nominal wheel radius. The lateral, longitudinal (i.e. in the circumferential direction) and radial resolutions of the scan were 0.03 mm. As the computational algorithm adopted in the in-house software (see Sect. 3) accounts for any generic deviation between the nominal wheel/rail profiles and the actual shape of the damage, the 3D scanned mesh needs to be post-processed in a format which is suitable for the software. The 3D scan was mapped in a matrix where the radial deviation from the nominal wheel profile for each square millimetre was stored. This deviation, which was obtained by interpolating between the

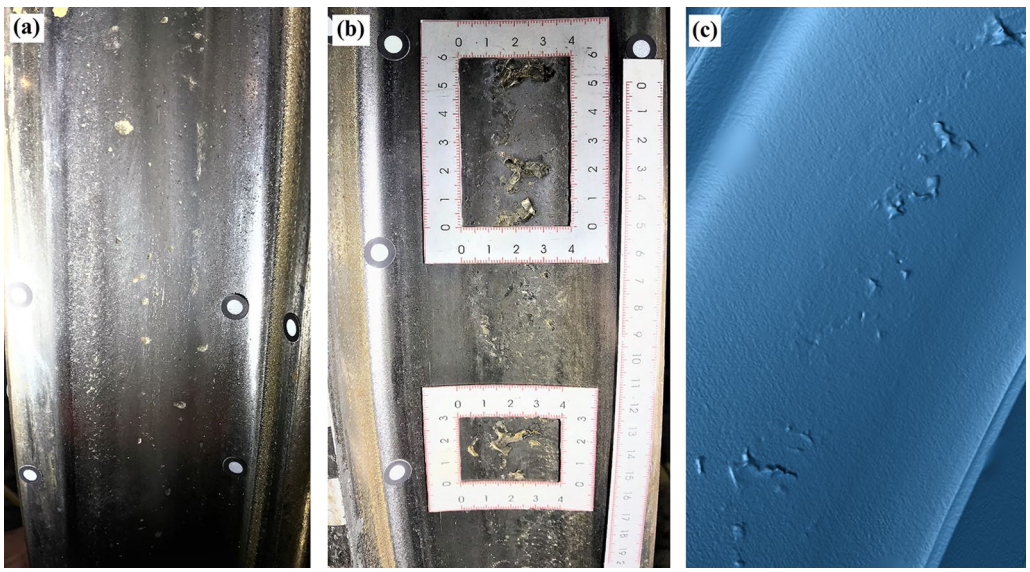

Fig. 2 Wheel tread sections of the **a** less damaged wheel and **b** severely damaged wheel of the wheelset studied in the field test, and **c** surface geometry generated from scanning of the severely damaged wheel

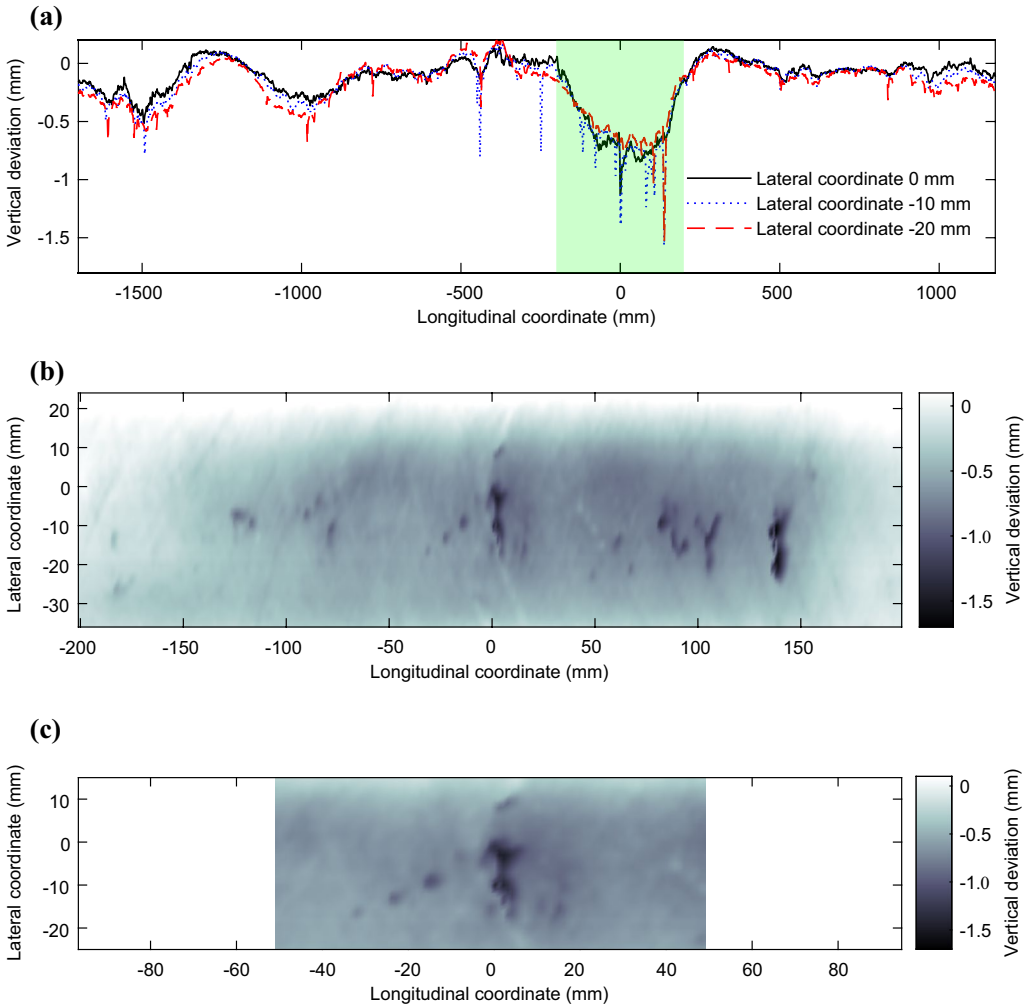

Fig. 3 Radial deviation from the average wheel profile for **a** three different lateral coordinates of the rolling circle, **b** the area of the wheel tread affected by wear and severe RCF, and **c** zoom-in of the most severe RCF damage. The nominal rolling circle is at lateral coordinate 0 mm. The interval of longitudinal coordinates of the area plotted in **b** is highlighted in green in **a**

radial deviations of the points contained on the scanned surface, had a resolution of 1 mm in the lateral and longitudinal directions. The scanning procedure allowed to identify e.g. RCF clusters, tread wear, wheel flats, etc.; however, it could not capture subsurface voids, inclusions and cracks. For this reason, RCF cracks were not accounted for in the scanned wheel surface, while all RCF clusters could be captured. After the mapping procedure was completed, a careful visual check was performed to ensure that the shape and dimensions of the defects were not altered.

The mesh generated for the area of the damaged wheel in Fig. 2b is shown in Fig. 3b, c. It is observed that the main contributions to the irregularities in the wheel tread come from the RCF damage clusters. However, the measurements also revealed an about 340 mm long defect, the shape of which resembles localised hollow wear, see Fig. 3b. The depth of the long defect increases gradually between the longitudinal coordinates − 140 and − 40 mm, while it more abruptly returns to levels close to the nominal profile between longitudinal coordinates 160 and 200 mm, see Fig. 3a, b. Thus, the shape of the long defect is not symmetric with respect to its centre, and different magnitudes of wheel–rail impact load can be expected depending on the rolling direction. The longitudinal coordinate has its origin at the centre of the RCF defect highlighted in Fig. 3c.

In the field test, the damaged wheelset had a static axle load of 14.5 t. The train was run in both directions over the impact load detector without being turned around. Thus, the severely damaged wheel always impacted on the same rail of the detector. Trials were performed at vehicle speeds 10 km/h (3 passages), 55 km/h (7 passages) and 100 km/h (6 passages). For each trial, the speed of the train, the mean loads and the peak loads generated by the passage of the

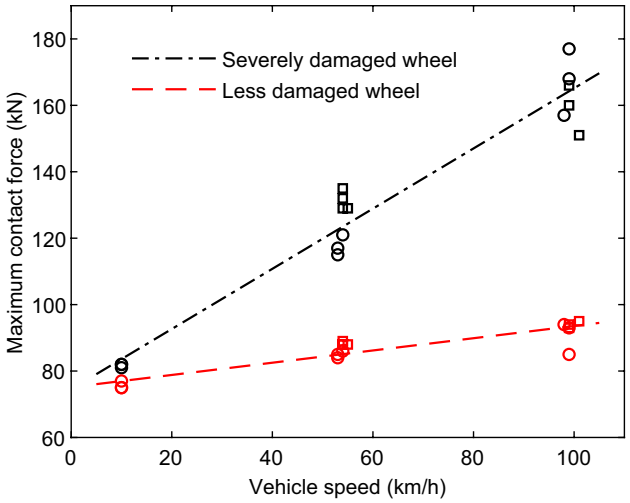

Fig. 4 Maximum wheel–rail contact forces (peak loads) measured at different speeds during the field test for vehicle travelling northbound (*circles*) or southbound (*squares*), and derived linear regression models

two wheels in the damaged wheelset were acquired from the wheel impact load detector.

During the field test, the start position of the vehicle with respect to the wheel impact load detector was chosen aiming for a repeatable and consistent position of impact within the detector for each test run. Unfortunately, this aim was found to only be achieved at train speeds up to 10 km/h. Since the train had to start at some kilometres away from the detector, the same alignment for consecutive test runs could not be maintained at higher speeds.

3.2 Measured wheel–rail impact loads

The results from the field test are seen in Fig. 4, where data in terms of maximum peak (impact) loads registered by the detector for the severely damaged wheel and the less damaged wheel are plotted using black and red markers, respectively. Circles and square markers are used to indicate the wheelset travelling direction; from Luleå to Boden (northbound) or from Boden to Luleå (southbound), respectively. For the severely damaged wheel, it was noticed that higher impact loads were registered at 55 km/h when the train was travelling southbound, while at 100 km/h higher loads were generally registered when the train was travelling nothbound [1]. Prior to the tests, the train starting position was chosen so that the damaged area of the wheel would hit the rail exactly at a point above one of the instrumented sleepers. However, perfect alignment was only achieved for the initial tests performed at 10 km/h [2].

Linear regression models for the two wheels in the wheelset were fitted to the results for the three speeds up to 100 km/h. These results indicate that impact loads registered for the damaged wheel show an increase of about 0.95 kN per km/h between 10 and 100 km/h [2], while the other wheel shows an increase of about 0.15 kN/(km/h). For the less damaged wheel, the minor increase in dynamic load with increasing speed is likely to be mainly influenced by the sleeper passing, or possibly by interaction with the severely damaged wheel via the axle (or even via the rails and sleepers). The minor increase in dynamic load confirms the hypothesis that the defects present on that wheel were only cosmetic. As the magnitudes of peak load produced by the less damaged wheel are not high enough to significantly contribute to wheelset deterioration, the simulations performed in this work will focus on impact loads generated by the severely damaged wheel.

3.3 Verification of in-house software

The field test results have been used to verify the in-house MATLAB software WERAN (WhEel\RAil Noise) originally developed in [21], and later expanded in [16]. The in-house software solves the non linear normal contact problem using the active set algorithm proposed by Kalker [22], while simulation of dynamic vehicle–track interaction is carried out in the time domain using a convolution integral approach. At the interface between the two bodies, including the irregularities in the wheel–rail contact, a potential contact area is defined and discretised into a mesh of rectangular elements. In each time step, the elements that are in contact and their contact pressures are determined through an iterative procedure. For each wheel, the total vertical wheel–rail contact force is computed by summing the contributions of contact pressure in all elements of the contact patch. The force is convoluted with pre-calculated Green's functions (impulse response functions) for the applied wheelset and track models to obtain the corresponding wheel and rail displacements in each contact. The iteration proceeds to the next time step when the displacements agree with the kinematic constraints.

The Green's functions for the wheelset and the track models are computed by means of an inverse Fourier transform of the complex-valued frequency response functions calculated at potential contact points of the wheelset and track models. For the track model, the relative motion between the wheelset and the track is accounted for by computing and assembling discrete moving Green's functions obtained from receptances at several rail positions up to a sufficient distance from the contact point. The receptances are established by use of finite element (FE) simulations. A full description of the simulation algorithm, as well as of the equations implemented in the software WERAN, is given in [16]. A shorter description can be found in [23].

The applied 3D periodic finite element (FE) model of a ballasted tangent track section was established using the

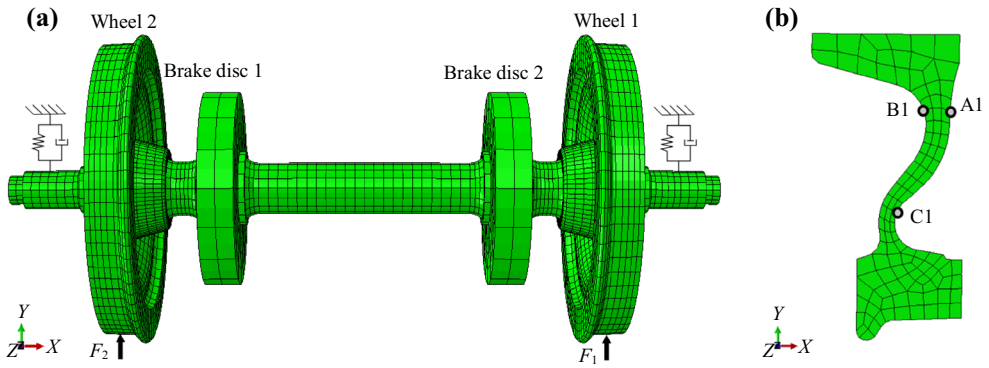

Fig. 5 **a** FE model of the wheelset used in the field test at Sunderbyn, and **b** cross-section of the wheel with positions of nodes where wheel stress transfer functions have been computed (see Sect. 5)

same parameters and input data as listed in [16]. The track model is characterised by concrete monobloc Abetong A22 sleepers and UIC60 rails. Each sleeper is modelled as a uniform Rayleigh-Timoshenko beam discretised using 20 elements of equal length, while each rail is modelled as a Rayleigh-Timoshenko beam with a discretisation of 8 elements per sleeper bay. The rail endings on the two sides of the track model have clamped boundary conditions [16]. Three different combinations of sleeper support bed moduli and viscous damping per unit area have been employed (60, 100 and 140 MN/m^3 and 50, 82 and 116 kNs/m^3, respectively) to investigate the influence of sleeper support stiffness on generated impact loads. The displacement frequency response functions for the track were computed up to 2500 Hz with a constant sampling frequency of 0.1 Hz.

Based on the design of the damaged wheelset used during the field test, a 3D FE model of the wheelset was established in Abaqus 2019 [24], see Fig. 5a. The wheels were modelled with a diameter of 920 mm (they had never been reprofiled before the field test) and the axle-mounted brake discs were included. Each axlebox was modelled as a reference point with an inertial mass of 100 kg located at the centre of the journal. Each primary suspension (with stiffness 1.2 MN/m and viscous damping 4 kNs/m in the vertical direction) was connected to a rigid reference and to the wheelset at the axlebox reference point. These reference points were tied to the external surface of the respective journals. The wheelset model was meshed using twenty-node quadratic brick elements referred to as C3D20R [24] and has 555,500 degrees of freedom (DOFs). The average element side length is 3 cm, but finer elements with side lengths of 1 cm were used at the axle fillets and in the wheel hub as well as in the vicinity of the nominal rolling circles on the wheel treads. The highest stresses are expected in these regions and, subsequently, these finer elements were used for the extraction of representative stress frequency response functions. Since quadratic elements were used, the actual distance between different nodes in the most critical areas of the wheelset is shorter than 1 cm. As the FE model of the wheelset was not used to compute wheel–rail contact stresses, it was not necessary to further refine the mesh in the vicinity of the wheel tread. The same material properties were used as for the wheelset model presented in [25]. Material damping was accounted for so that wheelset modes were damped with a damping ratio of about 1 percent. The displacement frequency response functions for several lateral positions of the wheel–rail contact (different rolling circles) were computed up to 2500 Hz with a constant sampling frequency of 0.01 Hz. Displacements and stress frequency response functions for the wheelset were computed in around 5 h (using two cores of an Intel i7 processor), while a simulation in WERAN for a vehicle running a distance of around 300 m required 25 min (using one core of the same processor).

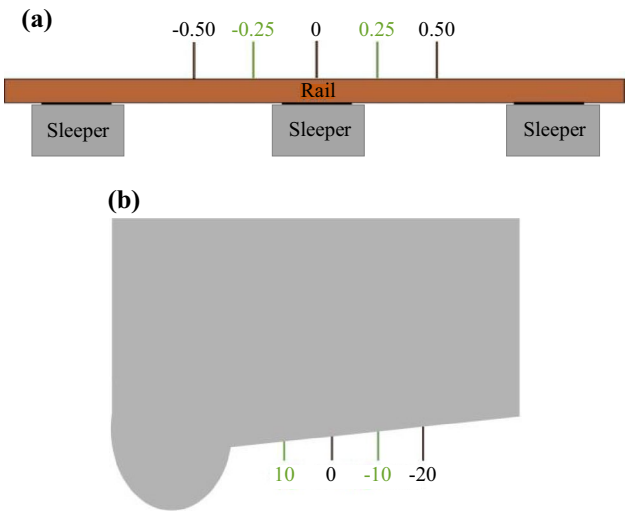

Fig. 6 Schematic descriptions of **a** normalised longitudinal position of wheel–rail impact within a sleeper bay and **b** lateral contact position (in mm) on the wheel tread. The sketches are not to scale

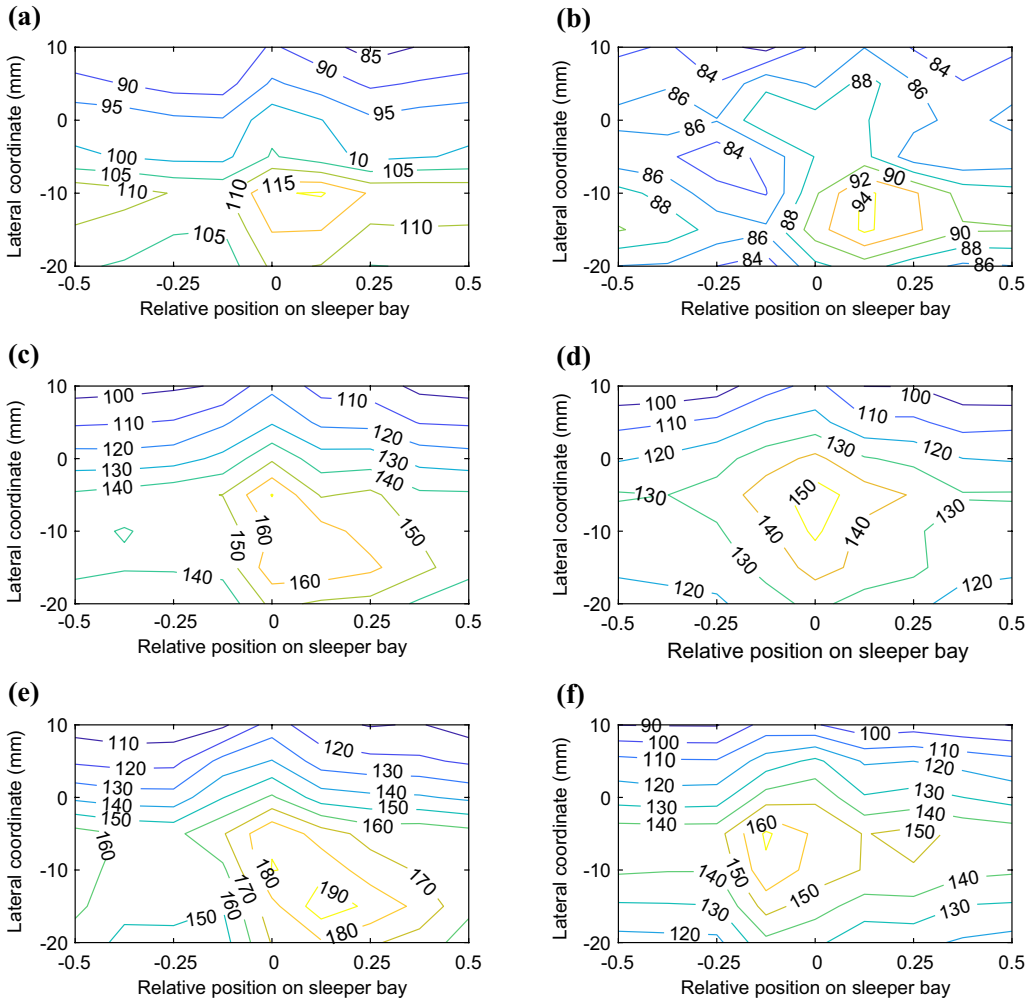

Fig. 7 Contour plot of calculated maximum vertical wheel–rail contact forces (in kN) generated by the wheel tread damage in Fig. 3. The results are based on simulations where the rolling circle was prescribed at seven equidistant lateral coordinates on the tread, while the prescribed longitudinal position of the trailing edge of the long defect (longitudinal coordinate 180 mm in Fig. 3) was aligned with eight equidistant positions centred around a sleeper (the sleeper is positioned at relative longitudinal coordinate 0). Vehicle speeds **a**, **b** 55 km/h, **c**, **d** 100 km/h and **e**, **f** 140 km/h, when **a**, **c**, **e** travelling northbound and **b**, **d**, **f** travelling southbound

Simulations were performed in the in-house software WERAN for different vehicle speeds, running directions of the train, and sleeper support parameters. Seven different lateral positions of the wheel–rail contact point were studied to investigate the influence of the 3D shape of the scanned wheel tread defect geometry on the predicted impact load. The prescribed lateral position of the contact was varied from lateral coordinate − 20 to + 10 mm (relative to the nominal rolling circle at 70 mm from the inside of the flange) at discrete intervals of 5 mm. Moreover, the effect of the position within the sleeper bay where the tread defect made impact with the rail was investigated by incrementally rotating the start position of the wheel. The prescribed normalised impact positions within the sleeper bay and lateral contact positions on the wheel tread are indicated in Fig. 6. All simulations described in this section have been performed for the case of running on a straight track, and for an axle load of 14.5 t, which corresponds to the mean loads registered by the WILD during the field test at Sunderbyn.

To account for the difference in dynamic wheel–rail interaction due to the unsymmetric wheel defects, see Fig. 3b, both directions of wheel revolution have been studied in the simulations: "travelling northbound", when the contact point moves from the left to the right in Fig. 3a and "travelling southbound" when the contact point moves from right to left. The small indentations on the opposite wheel as well as the surface roughness on the two rails have been neglected. This is motivated by the parameter studies presented in [25].

Figure 7 illustrates the influence of the lateral contact coordinate and sleeper bay position on the computed maximum wheel–rail contact forces for the damaged wheel in the field test at Sunderbyn. Negative coordinates mean that the

prescribed rolling circle has been shifted towards the field side of the wheel tread (the nominal rolling circle is at coordinate 0). The maximum force is generated when the level of the tread surface is returning to a nominal vertical position from a section where material has been removed by wear and RCF damage. Thus, the horizontal axis in the figure indicates the normalised position within a sleeper bay where the trailing edge of the long defect has been prescribed to meet the rail. When travelling northbound, this corresponds to the edge of the tread defect at longitudinal coordinate 180 mm, while it corresponds to the other edge at longitudinal coordinate − 140 mm when travelling southbound. The longitudinal position within the sleeper bay is indicated relative to the sleeper bay length and is zero above a sleeper and ± 0.5 at the centre of the two adjacent bays. For example, in Fig. 7e, it is observed that the maximum calculated force (here over 190 kN) is obtained when the rolling circle is at lateral coordinate − 15 mm and the trailing edge of the long defect meets the rail at a relative position of about 0.2, which corresponds to about 12 cm after the centre of the sleeper (sleeper distance 60 cm).

Figure 7 shows that calculated impact loads were higher when the train was travelling northbound (Fig. 7a, c, e). Here, the wheel–rail contact is subjected to a slower unloading phase when the contact point enters the long defect at its "smoother" edge, while the peak load is generated when the wheel centre trajectory quickly returns to its nominal level at the "sharper" edge. Interestingly, it can be observed that the highest forces were generated at a position towards the sloped ends of the long defect and not at the local RCF defects seen in Fig. 3c. This is discussed in more detail in Sect. 4.

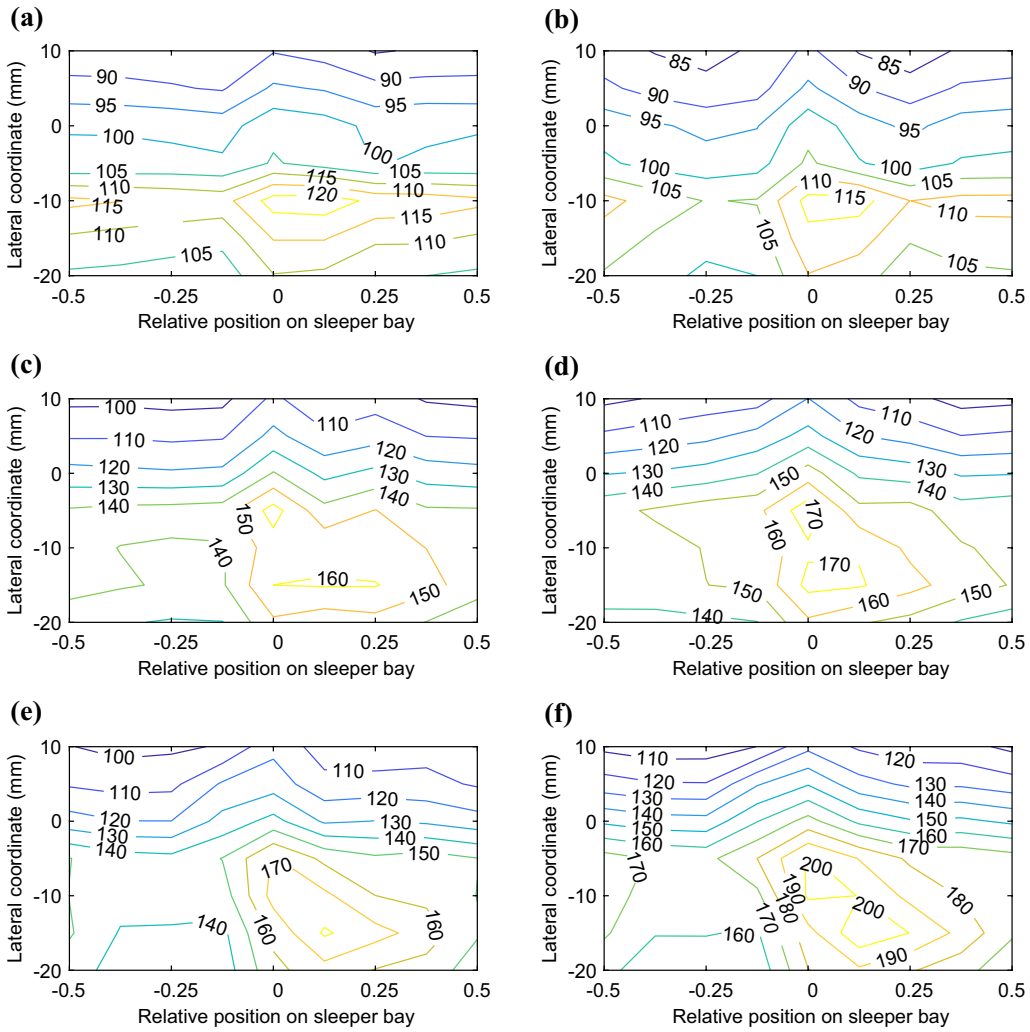

Fig. 8 Contour plot of calculated maximum vertical wheel–rail contact forces (in kN) generated by the wheel tread damage in Fig. 3. Vehicle speeds **a**, **b** 55 km/h, **c**, **d** 100 km/h and **e**, **f** 140 km/h, vehicle travelling northbound and sleeper bed modulus **a**, **c**, **e** 60 MN/m^3 and **b**, **d**, **f** 140 MN/m^3. See also caption to Fig. 7

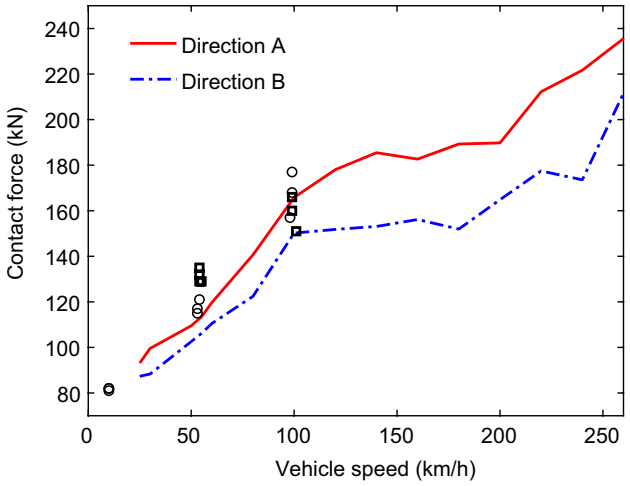

Fig. 9 Measured (*black circles* and *squares*) and simulated (*red* and *blue* lines) impact loads for the severely damaged wheel used in the field test at Sunderbyn when travelling northbound (black circles) or southbound (black squares). Results from simulations when travelling northbound (red solid line) or southbound (blue dashed-dotted line) are shown as average maximum impact loads registered at different speed values for four lateral coordinates of the rolling circle (0, − 5, − 10 and − 15 mm) and for sleeper support bed modulus 100 MN/m^3

Impact loads increased when vehicle speed was raised from 55 to 100 km/h and 140 km/h. In particular, this applies to impacts occurring in the vicinity of a sleeper. This result is in line with earlier studies performed using WERAN [16], and expected since the track stiffness is higher above sleepers. The highest wheel–rail contact forces were registered when the rolling circle was located towards the field side between lateral coordinates − 15 and 0 mm. This corresponds to a wheel centre trajectory influenced by the central deeper part of the long defect, see Fig. 3b, which implies that the impact load was mainly determined by the long defect.

The results in Fig. 7 were obtained using a track model with sleeper support bed modulus 100 MN/m^3. The corresponding results for two other sleeper support bed moduli (60 and 140 MN/m^3) are presented in Fig. 8. For the investigated wheel tread damage, the stiffer sleeper support leads to somewhat higher impact loads compared to the cases with softer support for vehicle speeds 100 km/h, see Fig. 8c, d, and 140 km/h, see Fig. 8e, f. However, lower impact loads were obtained at 55 km/h, see Fig. 8a, b. The magnitudes of impact load in Fig. 7a, c, e (sleeper support bed modulus 100 kN/m^3) are in between the results in Fig. 8a, c, e and b, d, f (sleeper support bed moduli 60 and 140 kN/m^3, respectively). For a given wheel tread damage, this illustrates that the influence of track stiffness on impact load is significant, especially at higher vehicle speeds. Track stiffness is expected to increase during winters in countries like Sweden where the winter season can be very cold, and therefore a seasonal effect on wheel–rail impact loads can be expected. At 140 km/h, the simulated difference in maximum impact load between sleeper support bed moduli 60 and 140 kN/m^3 (i.e., for a more than doubled bed modulus value) is in the order of 20 kN. On the other hand, for a given sleeper support bed modulus of 140 kN/m^3, the maximum impact load can be reduced by around 30 kN by reducing the speed from 140 to 100 km/h. Thus, the influence of track stiffness seems to be relatively smaller than the influence of vehicle speed.

In Fig. 9, the calculated impact loads from the parameter study presented in Figs. 7 and 8 are compared with the impact loads measured at Sunderbyn. In the simulations, the vehicle speed range has been extended up to 260 km/h. In particular, simulations have been performed for intermediate speeds not tested at Sunderbyn. Different lateral coordinates of the rolling circle and longitudinal positions of the wheel–rail contact at impact were accounted for, and both traffic directions were considered. Each plotted simulation result is the average maximum impact load registered for four lateral coordinates of the rolling circle (0, − 5, − 10 and − 15 mm) at a given vehicle speed.

The calculated impact loads show good agreement with the magnitudes and increasing trend found during the field test. In particular, the results at speeds close to 100 km/h match very well with the measured data. At vehicle speeds close to 55 km/h, the simulation results are on average somewhat lower than the corresponding measured values. The lower rate of increase in wheel–rail impact loads for increasing vehicle speeds between 40 and 60 km/h might be due to the dynamic wheel–rail interaction generated by tread defects whose shape is similar to that of a wheel flat. In this study, the so-called long defect has a form that to some extent can be described as similar to a wheel flat. Wheel flats often result in a non-linear increase of impact load with increasing speed and a local maximum in impact load at a relatively low train speed. For example, in Ref. [21], a 100 mm long and 0.9 mm deep wheel flat was found to generate a local minimum in impact load between 35 and 85 km/h. For speeds up to 100 km/h, the measured increase in impact load with increasing speed is confirmed and the simulation and experimental results match well. For simulated vehicle speeds between 100 and 200 km/h, the rate of the increase in impact load is reduced, to increase again at vehicle speeds higher than 200 km/h. This is also expected to be due to the effect of the long defect. A similar influence of vehicle speed on impact load magnitude has been observed in other works, see Refs. [25] and [21].

4 Impact loads generated by different tread defects

The scanned wheel tread damage is here investigated as a combination of the RCF defects and the long defect, i.e. the radial deviation from the nominal wheel radius over a longer

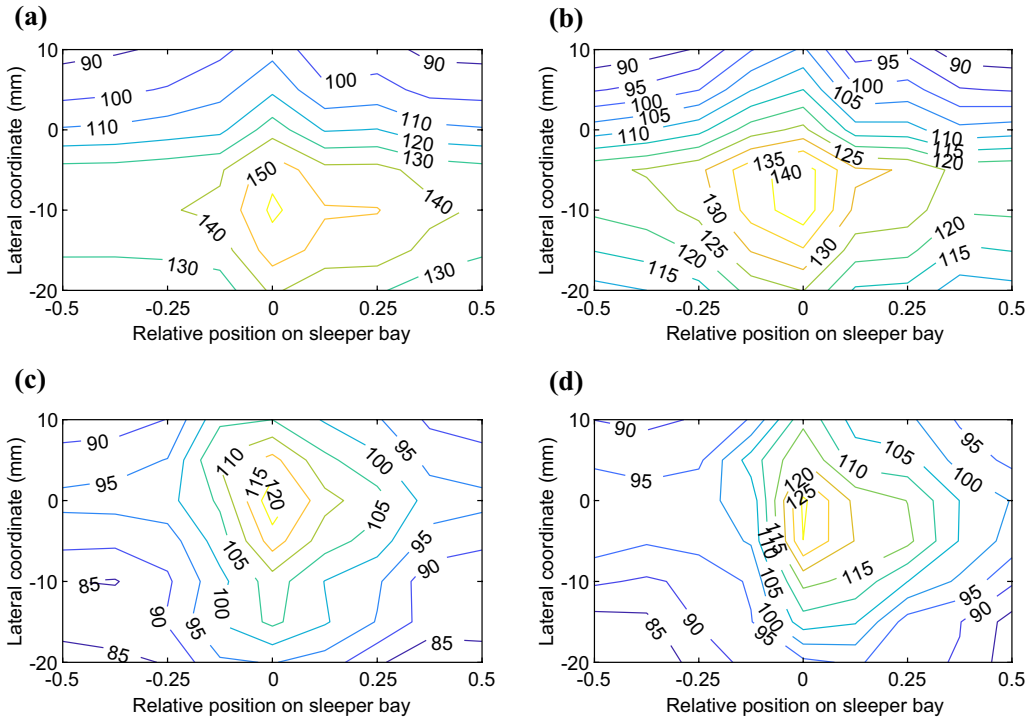

Fig. 10 Contour plot of calculated maximum vertical wheel–rail contact forces (in kN) generated by **a**, **b** the filtered surface of the long defect shown in Fig. 3, and **c**, **d** the RCF defects excluding the long defect. For the long defect, see caption to Fig. 7 for interpretation of the coordinates on the horizontal axis. For the RCF defects, the position of the centre of the defect at longitudinal coordinate 0 in Fig. 3b was aligned with different coordinates on the horizontal axis. Vehicle speed 100 km/h on straight track with sleeper bed modulus 100 MN/m^3. Travelling **a**, **c** northbound and **b**, **d** southbound

section of the tread. To compare the influence of the two different contributions to the overall tread defect, wheel–rail impact loads have been simulated for two post-processed versions of the scanned defect. Results related to impact load magnitudes are presented here, while consequences on wheelset durability are presented and discussed in Sect. 5.

To understand the influence of different types of surface damage, the mesh obtained from the 3D scans has been post-processed to separate the long defect from the RCF defects. To obtain the profile of the long defect, a median filter with a window size of 50 mm along the longitudinal coordinate and 10 mm along the lateral coordinate was applied such that the more abrupt variations in geometry (those due to the RCF defects) were filtered out. The geometry of the RCF defects was obtained by taking the difference between the scanned mesh and the filtered one. Calculated impact loads for different prescribed rolling circles and for both travelling directions are presented in Fig. 10. The results for the long defect are shown in Fig. 10a, b, while the corresponding results for the RCF defects are presented in Fig. 10c, d. Note that the approach to prescribe the longitudinal impact position of the RCF defects (Fig. 10c, d) was different compared to the approach used for the long defect (Fig. 10a, b). For the RCF defects, the position of the centre of the defect at longitudinal coordinate 0 in Fig. 3b was aligned with different positions in the sleeper bay, while the position of the trailing edge was used for the long defect.

These results can be compared to the corresponding contour plots in Fig. 7c, d for the original scanned surface of the damaged wheel. It is observed that the results for the filtered surface, see Fig. 10a, b, are very similar to those obtained for the original wheel surface, see Fig. 7c, d, although a relatively uniform reduction in impact loads by about 10 kN can be noted. On the other hand, the simulations only involving the RCF defects reached significantly lower impact load magnitudes.

Thus, it can be concluded that the long defect generates the dominating contribution to the high impact loads, whereas the influence of the various local RCF defects on the contact load magnitude is minor. It is observed that the RCF defect with the largest size and depth, which is centred at coordinates $(x', y') = (0, -8)$ mm, generates higher impact loads when the vehicle is travelling southbound, see Fig. 10d, compared to when it is travelling northbound, see Fig. 10d. This can be explained by the geometry of the defect leading to a steeper rise in wheel centre trajectory when travelling southbound, see Fig. 3c.

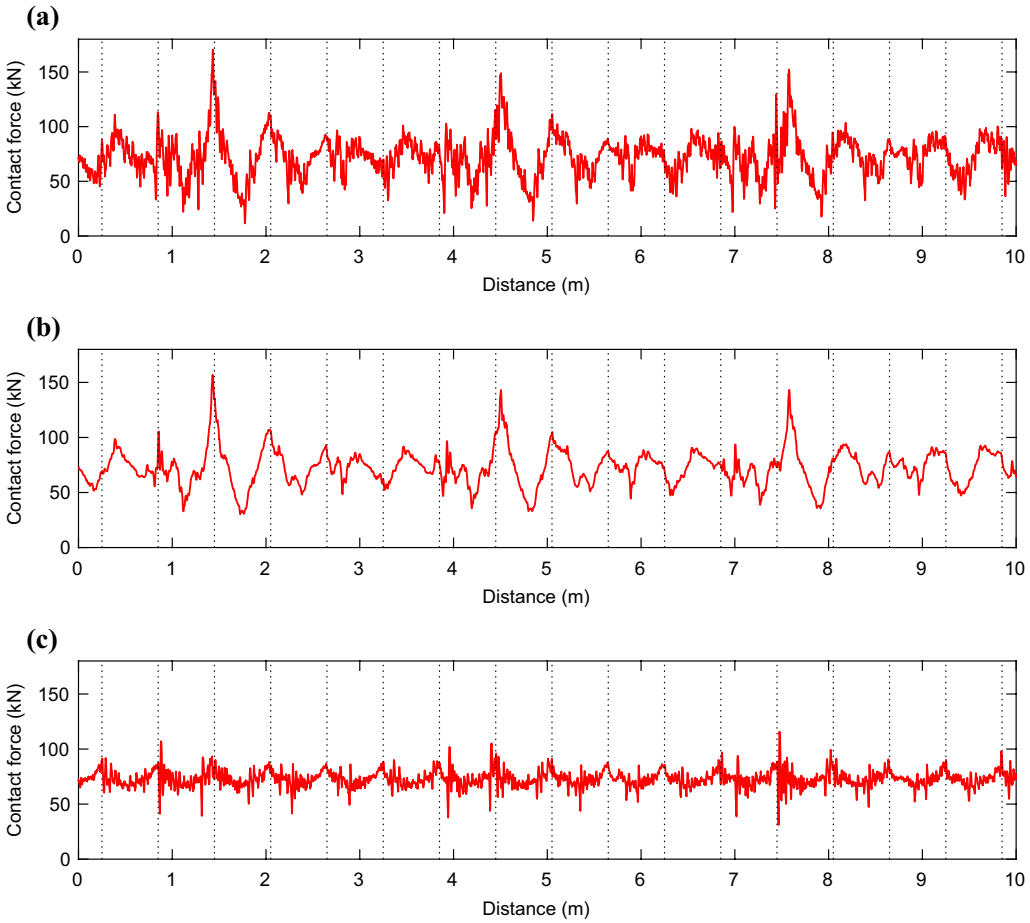

Fig. 11 Calculated time histories of vertical wheel–rail contact force: **a** original scanned surface geometry of the damaged wheel from the field test at Sunderbyn, **b** surface geometry of the same wheel filtered to remove the RCF defects, and **c** RCF defects on the same wheel. Train speed 100 km/h, sleeper support bed modulus 100 MN/m, travelling northbound, and rolling circle at lateral coordinate − 5 mm. The trailing edge of the **a**, **b** long defect and **c** deepest RCF damage were aligned with the sleeper located at 1.45 m from the start of the plot

The observation that the contribution of the long defect to the dynamic load is more severe than the contribution by the RCF clusters can be further confirmed by studying extracts of the simulated time histories of the vertical wheel–rail contact force, see Fig. 11. The original scanned surface of the severely damaged wheel at Sunderbyn was applied in the simulation presented in Fig. 11a, while results for the filtered surface and for the RCF defects are illustrated in Fig. 11b and c, respectively. In each figure, three wheel revolutions have been considered leading to a relatively periodic signature. It is clear that the force signature in Fig. 11a can be seen as a combination of the lower frequency trend (caused by the long defect) and higher frequency contributions (caused by the RCF damage and the general surface roughness). It was observed (not shown here) that the influence of the RCF damage was somewhat higher in the other travelling direction (about 10 kN higher when the defects hit adjacent to the sleeper), but still not significant relative to the contribution of the long defect. The reason why the RCF defects studied here lead to a relatively low contribution to the impact load can be attributed to the wheel–rail contact filter effect [26], which becomes significant when the projected surface of the tread defect is smaller or of the same order as the size of the wheel–rail contact area. This was confirmed in the parameter study presented in [25].

5 Effects on wheelset durability

Simulated wheel–rail contact force histories for damaged wheels can be used to assess the risk for fatigue damage in different locations of the wheelset. In previous studies [16, 25, 27], time histories of contact forces were used to assess the variations of bending stresses in different locations of a railway axle. The present work instead focuses on the wheels and bearings. The studies presented in this section still correspond to the wheelset used in the field test at Sunderbyn, see Fig. 4. However, the axle load in the

simulations has been increased to 20 t, which is a realistic axle load for a fully loaded passenger coach.

To focus on the effect of a few but significant cases, the results in this chapter feature a "worst case scenario" with respect to the calculated vertical forces. For each analysed wheel tread defect, the worst possible combination of lateral position of the contact point and rolling direction of the vehicle was employed. The analyses were limited to a vehicle speed of 100 km/h and a track model with sleeper support stiffness 100 MN/m^3. Results are compared to a "reference case" for a vehicle with nominal wheel profiles (i.e. with no tread damage or wear), where variations in the vertical wheel–rail contact forces are only due to the sleeper passing. The rails are assumed to be perfectly smooth and the time histories of the vertical wheel–rail contact forces are computed for straight track over a distance of 500 sleeper bays (about 103 wheel revolutions), which was found to be sufficient to obtain a robust statistical distribution of simulated wheel–rail contact forces and stresses.

Four operational cases have been studied. The reference case is labelled as "no damage". The "scanned damage" case corresponds to a vehicle running northbound (see Sect. 3) with a wheel having the tread profile that was scanned during the field tests at Sunderbyn. In the "long damage" case, the vehicle runs northbound with a wheel having the filtered damaged tread geometry. The "RCF damage" case features a wheel tread geometry only including RCF defects and wheel surface roughness. Since the latter type of damage generated higher wheel–rail contact forces when the vehicle was travelling southbound, see Fig. 10c, d a southbound train ride was simulated for this case.

A method to compute wheelset stresses based on pre-computed wheel–rail contact forces is presented in Ref. [16] and verified against measurements in a full-scale field test in Ref. [25]. Here, this method has been used to assess the effect of simulated contact forces generated by different defects on the wheel durability. To this end, time-variant stresses at selected locations in the wheelset were calculated in a post-processing step. The applied formulation was based on pre-computed stress frequency response functions, which were transformed into stress Green's functions by means of inverse Fourier transforms. Stress frequency response functions were computed up to 10 kHz at a sampling frequency of 0.05 Hz. The time histories for the six stress components in the studied points were determined by convoluting the time histories of the contact forces at the two wheel–rail contact points with their respective stress Green's functions.

5.1 Wheel web

Three different locations on the wheel web have been studied, see Fig. 5b. These areas of the wheel web affected by the highest principal stress ranges were identified based on static FE simulations accounting for both lateral and vertical wheel–rail contact loads at positions, and with magnitudes and directions, according to the European standard EN 13979-1 [28]. Then, the single nodes in those areas where the highest stresses due to dynamic variations in wheel–rail contact forces occurred were identified by applying the stress convolution procedure using the contact force time history plotted in Fig. 11a.

Two of these locations are closer to the wheel hub and are respectively affected by tensile stresses (node A1) and compressive stresses (node B1) when the wheel is subjected to a static vertical loading at the nominal rolling circle. The third location (node C1) is close to the wheel rim and mainly affected by compressive stresses. To approximately account for the influence of wheel rotation, also stresses at the three radially opposite positions on the wheel webs (nodes A2, B2 and C2) were considered.

Based on the calculated vertical wheel–rail contact forces, stress time histories at the six nodes (A1 to C2) for the four studied cases were computed. By alternating data from each pair of nodes (e.g. A1 and A2) every half wheel revolution, stress histories in terms of stress ranges for single locations on the wheel (location "A" in this example) were obtained. These time histories were then employed to evaluate the Dang Van equivalent stress $\sigma_{\mathrm{eq,dv}}$ as

$$\sigma_{\mathrm{eq,dv}}(t) = \tau_{\mathrm{Tr,a}}(t) + c_{\mathrm{dv}}\sigma_{\mathrm{h}}(t), \tag{1}$$

where c_{dv} is a non-dimensional material constant ($c_{\mathrm{dv}} = 1/3$ in this work), σ_{h} is the hydrostatic stress, and $\tau_{\mathrm{Tr,a}}$ is the Tresca shear stress computed from the "amplitudes" (deviations from mid values during the entire stress history) of the deviatoric stress tensor:

$$\tau_{\mathrm{Tr,a}}(t) = \frac{\sigma^{\mathrm{d}}_{1,\mathrm{a}}(t) - \sigma^{\mathrm{d}}_{3,\mathrm{a}}(t)}{2}, \tag{2}$$

where $\sigma^{\mathrm{d}}_{1,\mathrm{a}}$ and $\sigma^{\mathrm{d}}_{3,\mathrm{a}}$ are the maximum and minimum eigenvalues of the tensor of deviatoric stress "amplitude". The term $\langle c_{\mathrm{dv}}\sigma_{\mathrm{h}}(t)\rangle$ in Eq. (1) employs Macaulay brackets, meaning it is only accounted for when it has a positive value. The results obtained for the three studied wheel web locations and for the four damage cases are presented in Fig. 12a. It can be observed that the Dang Van stresses increase at all studied locations when damage is added to the wheel tread. In some cases, for example for location "C" towards the rim, the increase is more pronounced. Note that although the contact force time history for the case with the "long damage" contains slightly lower peak impact loads relative to the case "scanned damage", higher Dang Van stresses were registered at some locations for this case. This can be due to the fact that the frequency contents of each time-variant contact force cause excitation of different vibration modes, which

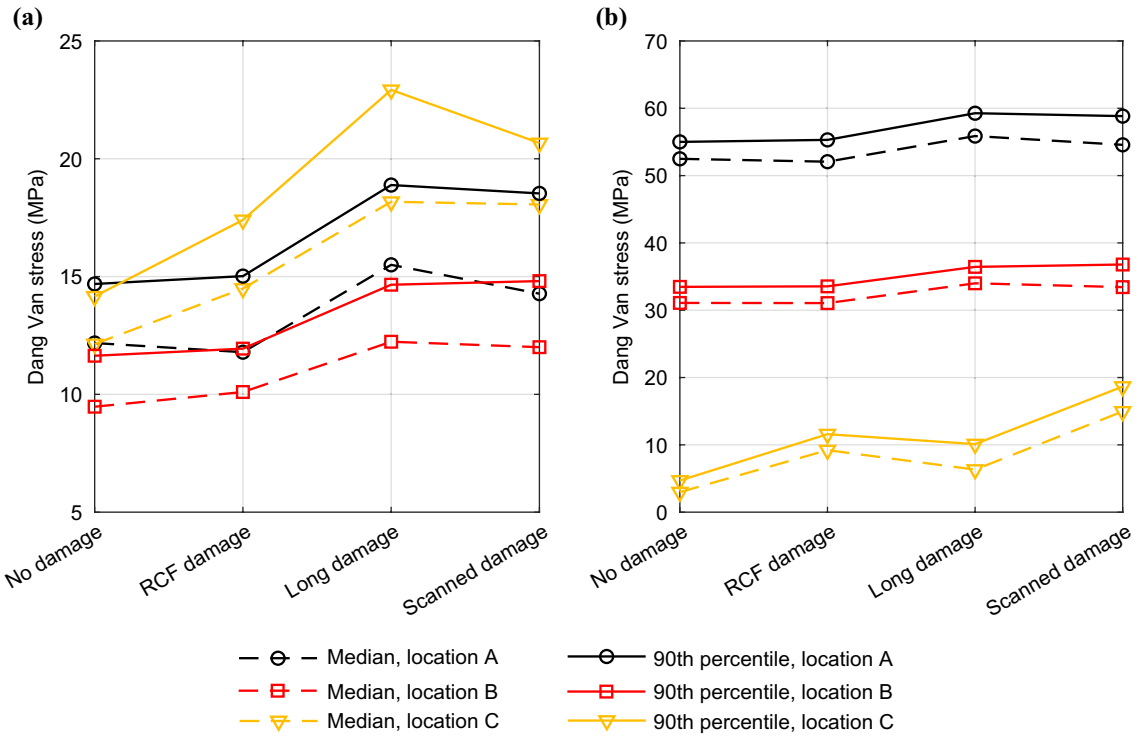

Fig. 12 Median (dashed-dotted lines) and 90th percentile (solid lines) of Dang Van stresses computed for the wheel web locations "A" (black lines with circles), "B" (red lines with squares) and "C" (yellow lines with triangles) simulated for the four types of damage for a vehicle running on **a** tangent track or **b** curved track

may generate higher stresses in some wheel locations. Overall, it can be noticed that the 90th percentile of the Dang Van stress in the three studied locations increases by between some 25% to 50% as compared to the undamaged wheel. Note, however, that stress levels are still low.

In order to further assess the impact of dynamic wheel stresses due to tread damage, static stresses from a curving

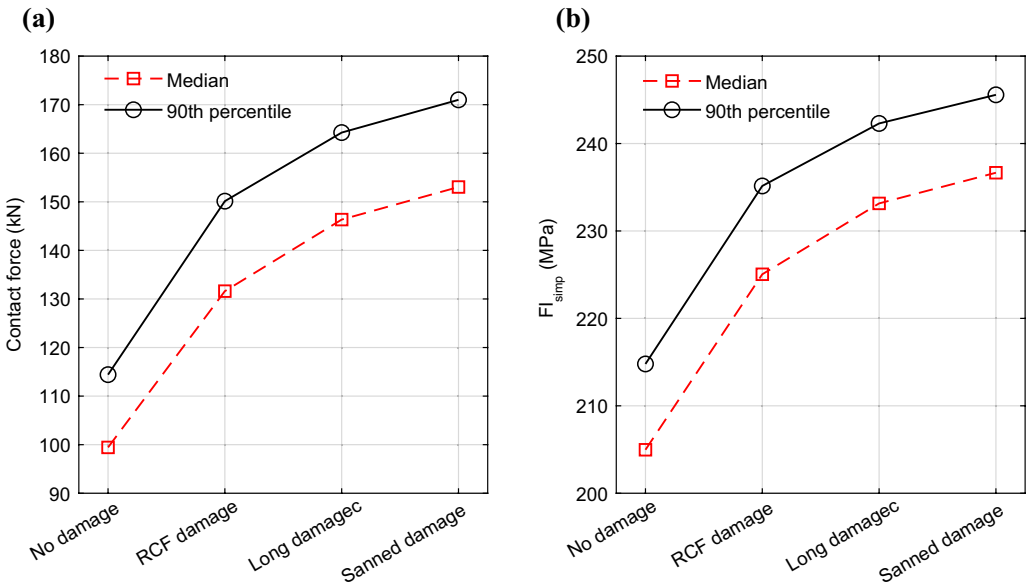

Fig. 13 Median and 90th percentile of **a** the vertical wheel–rail contact force and **b** the subsurface fatigue index FI_{simp} for the highest loaded material point in the four damage cases

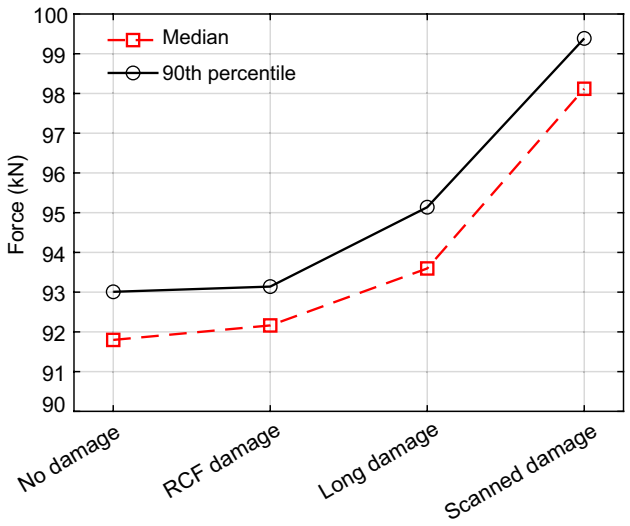

Fig. 14 Median and 90th percentile of the total vertical load acting on the bearing

scenario featuring a constant lateral wheel–rail contact force have been superposed on the stresses due to the wheel–rail impact. The static stresses were computed in a quasistatic FE analysis. To this end, a constant lateral force Y with magnitude 6 kN ($Y = 0.6P$, where $P = 100$ kN is the static wheel vertical load) was applied to the flange of the wheel according to the guidelines in EN 13979-1 [28].

Results are plotted in Fig. 12b. For locations "A" and "B", the increase in Dang Van stresses as compared to the undamaged wheel is around 10% (slightly less than 5 MPa), although this increase starts from a significantly higher value and can therefore be more significant for fatigue initiation. For location "C", it seems from Fig. 12a and b that the magnitudes of Dang Van stresses decrease when the lateral load is applied. This is due to the shift from a mainly compressive stress state when only a vertical load is applied to a mostly tensile stress state when the lateral load is added.

5.2 Wheel tread subsurface fatigue

Rolling contact fatigue is one of the principal failure modes for rolling surfaces [29]. In subsurface-initiated fatigue, cracks can be generated below the surface starting from material imperfections such as inclusions, voids or microstructural in homogeneities [29]. In railway wheels, these cracks tend to form at depths between 3 and 10 mm from the contact surface [30] and may grow towards the wheel tread or the hub. High contact load magnitudes due to damaged wheel treads or corrugated rails increase the risk of occurrence of subsurface fatigue.

In [30], a fatigue index for subsurface-initiated RCF was derived from the Dang Van equivalent stress. In order to derive a fatigue index that can be extended to cases in which the contact patch may be non-Hertzian and that can be easily used in real time to predict initiation of subsurface RCF, a simplified criterion was developed in [31]. The simplified subsurface-initiated RCF index index $\mathrm{FI}_{\mathrm{simp}}$ is defined as

$$\mathrm{FI}_{\mathrm{simp}} = 4.42 \times 10^6 \times \sqrt[3]{F}, \tag{3}$$

where F is the vertical load. Note that the derivation presumes nominal wheel–rail profiles, which is not the case in the current study. Derived stresses should thus mainly be considered for comparisons between different operational scenarios. For the wheelset analysed in the present work, $\mathrm{FI}_{\mathrm{simp}}$ has been computed using the time history of the wheel–rail contact force F for each of the four studied cases of damage.

The point of the wheel tread where the most significant damage is located (the trailing edge for the long defect and the location of the deepest defect for the RCF cluster) has been tracked throughout the four simulations. Values of the vertical wheel–rail contact force, as well as of $\mathrm{FI}_{\mathrm{simp}}$, in time windows when these points are in contact with the rail have been extracted. This resulted in 103 (one per wheel revolution) values of the vertical contact force and $\mathrm{FI}_{\mathrm{simp}}$, respectively. According to a convergence study, this travelling distance produces a representative statistical distribution of the loading of the studied wheel point. The loading distributions which were obtained by running either about 50 or about 200 wheel revolutions did not show any significant differences.

The median values and the values corresponding to the 90th percentile of the obtained distributions of contact forces and $\mathrm{FI}_{\mathrm{simp}}$ are plotted in Fig. 13 for the four studied cases. As expected, $\mathrm{FI}_{\mathrm{simp}}$ increases with increasing levels of contact force. However, due to the cubic root in Eq. 3, an increase of around 50% in contact force for the scanned damage leads to an increase of about 14% in $\mathrm{FI}_{\mathrm{simp}}$. On the other hand, due to the exponential nature of fatigue damage, a relatively small increase in $\mathrm{FI}_{\mathrm{simp}}$ can lead to a significant shortening of the fatigue life of the wheel rim if the fatigue limit is exceeded.

5.3 Bearings

Fatigue of bearings has been assessed based on the force in the primary suspension simulated for the four cases of tread damage. The bearings installed on the Sunderbyn field test wheelset were assumed to be cylindrical roller bearings (common for non-powered trailer wheelsets). This implies that axial loads can be neglected in the following simplified life calculation according to the SKF railway technical handbook [32]. The procedure followed in this paper adopts a simplified theory and only accounts for vertical forces acting on the axle boxes. A more complete calculation procedure (which is, however, applied to tapered roller bearings

mounted on a wheelset affected by wheel-polygonal wear) is presented in [33].

Here, the vertical force on the bearing is assessed based on the time histories of vertical displacement and velocity of the axlebox adjacent to the damaged wheel. It was computed by applying the convolution integral approach to the simulated wheel–rail contact force, using displacement frequency response functions computed up to 2500 Hz for the axlebox reference point in the FE wheelset model. Thus, the total (static and dynamic) vertical force acting on the bearing has been derived as

$$F(t) = k_{\mathrm{s}} \cdot y_{\mathrm{axlebox}}(t) + c_{\mathrm{d}} \cdot \frac{\mathrm{d}y_{\mathrm{axlebox}}(t)}{\mathrm{d}t}, \tag{4}$$

where k_{s} and c_{d} are the stiffness and viscous damping of the primary suspension, respectively, and $y_{\mathrm{axlebox}}(t)$ is the vertical displacement of the axlebox. For the four analysed cases, the median and the 90th percentile of the bearing force are shown in Fig. 14. It can be observed that the relative increase between the cases of no damage and the worst case ("scanned damage") is only 7% The increase in bearing force may thus seem less relevant compared to the corresponding increase in wheel–rail contact force. However, as mentioned for the other wheelset components, rather small increases in loading can lead to significant variations in the resulting fatigue life if the conditions are such that the fatigue limit is exceeded.

The results in Fig. 14 have been compared to the calculation procedure in the guidelines from the SKF railway technical handbook [32]. According to that procedure, dynamic bearing loads between 8.3 and 10.9 kN can be expected for bearings of a damaged wheelset similar to the one used in the field test at Sunderbyn (i.e. non-powered wheelset for a passenger coach with 20-t axle load). The results plotted in Fig. 14 for the worst types of damage are found to be in line with the handbook guidelines. The simulation results are in line with the static load acting on the bearings (9.2 t).

6 Concluding remarks

A field test with a train running at different speeds over a wheel impact load detector has been described. One of the wheelsets in the train had severe wheel tread damage. The 3D geometry of the defect, including a large area on the wheel tread affected by RCF damage, was scanned by means of laser and its characteristics have been described. The measured geometry and impact loads were used to verify an in-house model for simulating dynamic wheel–rail interaction. Based on the verified simulation model, the relation between impact load and various operational parameters (speed and travelling direction of the vehicle, position in the sleeper bay where the defect strikes the rail, lateral position of the wheelset and track stiffness) has been presented. Both the field test and the simulations have shown that impact loads due to the studied wheel tread damage increase with increasing train speeds up to 100 km/h. However, for higher speeds, a different behaviour could be observed. Higher track stiffness (which may be due to a higher sleeper support bed modulus or a shorter distance between a sleeper and the position of impact) can cause a visible increase in impact loads. Wheelset stresses have been computed for different forms of scanned tread damage, and the impact on the durability of wheel discs, wheel rims and bearings has been assessed. It was shown that tread damage leads to a significant increase in wheelset stresses when the vehicle is travelling on straight track. Nevertheless, this increase is lower than the corresponding stress generated by the quasi-static lateral contact forces during curving.

Acknowledgements The current work is part of the activities within the Centre of Excellence CHARMEC (CHAlmers Railway MEChanics, www.chalmers.se/charmec). Parts of the study have been funded from the European Union's Horizon 2020 research and innovation programme in the project In2Track3 under grant agreement No. 101012456. The authors are grateful to Dr Matthias Asplund from Trafikverket and Mr Pär Söderström from SJ for arranging the field test and for sharing data and results.

References

1. Asplund M (2018) Provkörning med hjulskada över hjulskadedetektor (Test run with wheel tread damage over a wheel damage detector). Technical report, Trafikverket, Luleå, Sweden, p 18 (in Swedish)
2. Asplund M, Söderström P (2022) Field validation of force response from defective wheel. In: Proceedings of the 12th international conference on contact mechanics and wear of rail/wheel systems (CM2022), Melbourne, Australia, 4–7 Sept 2022, p 5
3. Andersson R, Ahlström J, Kabo E, Larsson F, Ekberg A (2018) Numerical investigation of crack initiation in rails and wheels affected by martensite spots. Int J Fatigue 114:238–251
4. Krishna VV, Hossein-Nia S, Casanueva C, Stichel S, Trummer G, Six K (2022) Rail RCF damage quantification and comparison for different damage models. Railw Eng Sci 30(1):23–40
5. Nielsen JCO, Pieringer A, Thompson D, Torstensson P (2021) Wheel–rail impact loads, noise and vibration: a review of excitation mechanisms, prediction methods and mitigation measures. In:

Degrande G et al (ed) Noise and vibration mitigation for rail transportation systems (Proceedings of the 13th international workshop on railway noise; 2019; Ghent, Belgium). Notes on numerical fluid mechanics and multidisciplinary design. Springer, Cham, pp 3–40
6. Bosso N, Magelli M, Zampieri N (2022) Simulation of wheel and rail profile wear: a review of numerical models. Railw Eng Sci 30(4):403–436
7. Liao X, Yi C, Zhang Y, Chen Z, Ou F, Lin J (2022) A simulation investigation on the effect of wheel-polygonal wear on dynamic vibration characteristics of the axle-box system. Eng Fail Anal 139:106513
8. Hou Y, Wang X, Sun S, Que H, Guo R, Lin X, Jin S, Wu C, Zhou Y, Liu X (2023) Measured load spectra of the bearing in high-speed train gearbox under different gear meshing conditions. Railw Eng Sci 31(1):37–51
9. Mazzù A, Solazzi L, Lancini M, Petrogalli C, Ghidini A, Faccoli M (2015) An experimental procedure for surface damage assessment in railway wheel and rail steels. Wear 342–343:22–32
10. Van Dyk B, Edwards J, Dersch M, Ruppert C, Barkan C (2017) Evaluation of dynamic and impact wheel load factors and their application in design processes. Proc Inst Mech Eng Part F J Rail Rapid Transit 231(1):33–43
11. Riley Edwards J, Cook A, Dersch M, Qian Y (2018) Quantification of rail transit wheel loads and development of improved dynamic and impact loading factors for design. Proc Inst Mech Eng Part F J Rail Rapid Transit 232(10):2406–2417
12. Stratman B, Liu Y, Mahadevan S (2007) Structural health monitoring of railroad wheels using wheel impact load detectors. J Fail Anal Prev 7(3):218–225
13. Tao G, Wen Z, Jin X, Yang X (2020) Polygonisation of railway wheels: a critical review. Railw Eng Sci 28(4):317–345
14. Mishra S, Sharan P, Saara K (2022) Real time implementation of fiber Bragg grating sensor in monitoring flat wheel detection for railways. Eng Fail Anal 138:106376
15. Sresakoolchai J, Kaewunruen S (2021) Detection and severity evaluation of combined rail defects using deep learning. Vibration 4(2):341–356
16. Maglio M, Pieringer A, Nielsen JCO, Vernersson T (2021) Wheel–rail impact loads and axle bending stress simulated for generic distributions and shapes of discrete wheel tread damage. J Sound Vib 502:116085
17. Deuce R (2007) Wheel tread damage—An elementary guide. Technical report 100115000, Bombardier Transportation GmbH, Germany, p 38
18. Deuce R, Ekberg A, Kabo E (2019) Mechanical deterioration of wheels and rails under winter conditions–mechanisms and consequences. Proc Inst Mech Eng Part F J Rail Rapid Transit 233(6):640–648
19. HandySCAN (2023) VX inspect and VX model. Creaform, Canada. https://www.creaform3d.com/en. Accessed 7 Mar 2023
20. Mathworks (2021) MATLAB R2021b Documentation, USA. https://se.mathworks.com/help/matlab/. Accessed 7 Mar 2023
21. Pieringer A, Kropp W, Nielsen JCO (2014) The influence of contact modelling on simulated wheel/rail interaction due to wheel flats. Wear 314(1–2):273–281
22. Kalker J (1990) Three-dimensional elastic bodies in rolling contact. Kluwer Academic Publishers, Dordrecht
23. Maglio M (2023) Influence of railway wheel tread damage and track properties on wheelset durability—Field tests and numerical simulations. Dissertation, Chalmers University of Technology, Gothenburg, Sweden
24. Simulia (2019) Abaqus 2019 User Guide. Dassault Systemes, France
25. Maglio M, Vernersson T, Nielsen JCO, Pieringer A, Söderström P, Regazzi D, Cervello S (2022) Railway wheel tread damage and axle bending stress—Instrumented wheelset measurements and numerical simulations. Int J Rail Transp 10(3):275–297
26. Lundberg OE, Nordborg A, Lopez Arteaga I (2016) The influence of surface roughness on the contact stiffness and the contact filter effect in nonlinear wheel–track interaction. J Sound Vib 366:429–446
27. Maglio M, Kabo E, Ekberg A (2022) Railway wheelset fatigue life estimation based on field tests. Fatigue Fract Eng Mater Struct 45(9):2443–2456
28. European committee for standardization CEN (2011) Standard No. EN 13979-1:2003+A2 Railway applications—Wheelsets and bogies—Monobloc wheels—Technical approval procedure—Part 1: forged and rolled wheels. Brussels, p 60
29. Johnson K (1989) The strength of surfaces in rolling contact. Proc Inst Mech Eng C J Mech Eng Sci 203:115–163
30. Ekberg A, Kabo E, Andersson H (2002) An engineering model for prediction of rolling contact fatigue of railway wheels. Fatigue Fract Eng Mater Struct 25(1):899–909
31. Kabo E, Enblom R, Ekberg A (2011) A simplified index for evaluating subsurface initiated rolling contact fatigue from field measurements. Wear 271(1–2):120–124
32. SKF Group (2011) Railway technical handbook—Volume 1—Axleboxes, wheelset bearings, sensors, condition monitoring, subsystems and services. SKF, Sweden
33. Wang Z, Allen P, Mei G, Wang R, Yin Z, Zhang W (2020) Influence of wheel-polygonal wear on the dynamic forces within the axle-box bearing of a high-speed train. Veh Syst Dyn 58(9):1385–1406